Forschungszentrum Jülich GmbH
Institute of Complex Systems

Lecture Notes of the
42nd IFF Spring School 2011

Jan K.G. Dhont, Gerhard Gompper, Peter R.Lang,
Dieter Richter, Marisol Ripoll, Dieter Willbold, Reiner Zorn (Eds.)

Macromolecular Systems in Soft and Living Matter

This Spring School was organized
by the Institute of Complex Systems
of the Forschungszentrum Jülich
on 14 – 25 February 2011

In collaboration with
universities and research institutes.

Schriften des Forschungszentrums Jülich
Reihe Schlüsseltechnologien / Key Technologies Band / Volume 20

ISSN 1866-1807 ISBN 978-3-89336-688-0

D 3 Blood cells and blood flow

D. A. Fedosov
Institut für Festkörperforschung
Forschungszentrum Jülich GmbH

Contents

1 Introduction

Blood is circulated around the entire body performing a number of physiological functions. Its main functions are the transport of oxygen and nutrients to cells of the body, removal of waste products such as carbon dioxide and urea, and circulation of molecules and cells which mediate the organism's defense and immune response and play a fundamental role in the tissue repair process. Abnormal blood flow is often correlated with a broad range of disorders and diseases which include hypertension, anemia, atherosclerosis, malaria, and thrombosis. Understanding the rheological properties and dynamics of blood cells and blood flow is crucial for many biomedical and bioengineering applications. Examples include the development of blood substitutes, the design of blood flow assisting devices, and drug delivery. In addition, understanding of vital blood related processes in health and disease may aid in the development of new effective treatments.

Blood is a physiological fluid that consists of erythrocytes or red blood cells (RBCs), leukocytes or white blood cells (WBCs), thrombocytes or platelets, and plasma containing various molecules and ions. RBCs constitute approximately 45% of the total blood volume, WBCs around 0.7%, and the rest is taken up by blood plasma and its substances. One microliter of blood contains about 5 million RBCs, roughly 5 thousand WBCs, and approximately a quarter million platelets.

Figure 1 shows a scanning electron micrograph of blood cells. Human RBCs have a relatively

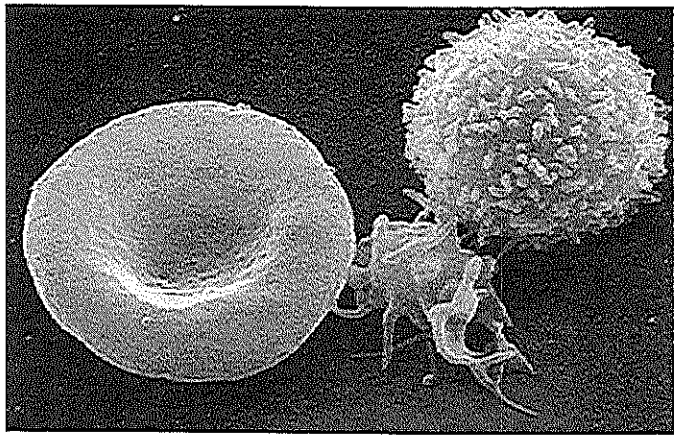

Fig. 1: *A scanning electron micrograph of blood cells. From left to right: human erythrocyte, thrombocyte (platelet), leukocyte.*

simple structure in comparison to other cells. RBCs resemble biconcave disks and contain a viscous cytosol enclosed by a membrane. At the stage of the RBC formation, the nucleus and other organelles that are generally present in other eukaryotic cells are ejected, leaving behind a relatively homogeneous cytoplasm and no inner cytoskeleton. RBC cytoplasm is a hemoglobin rich solution, which is able to bind oxygen. Therefore, the main RBC function is oxygen supply and delivery to body tissues. RBCs are extremely deformable and can pass through capillaries with a diameter several times smaller than the RBC size.

In comparison to RBCs, WBCs have one or multiple nuclei, are stiffer than RBCs and have a spherical shape. WBCs are an important part of the body's immune system. They protect the body against invading bacteria, parasites, and viruses by killing these microorganisms through phagocytosis ingestion and other antigen-specific cytotoxic mechanisms. There exist different types of leukocytes (e.g., neutrophils, eosinophils, basophils, monocytes, and lymphocytes), each of which is designed to fight a specific type of infection.

Freely circulating WBCs are able to adhere to the vascular endothelium, which is a crucial step in the immune response [1]. Rolling along the vessel wall allows WBCs to efficiently monitor for potential molecular signals, since the rolling velocity at the vessel wall is much smaller than that of the blood flow. In fact, microfluidic experiments [2] showed that WBCs adhere only above a critical threshold of shear. Firm adhesion of leukocytes is generally recognized as the final step of the WBC adhesive dynamics within a vessel with further cross-endothelium migration into the surrounding tissue.

In this chapter we present a cell model [3, 4] which is constructed by a network of viscoelastic springs combined with bending energy and constraints for surface-area and volume conservation. The model is used within the framework of the Dissipative Particle Dynamics (DPD) method [5] (see appendix A for details) and is able to reproduce realistic mechanical and rheological properties and dynamics of blood cells. Simulation results include several single cell tests, blood flow in microtubes ranging from 10 to 40 microns in diameter, and WBC adhesive dynamics, and are compared with available experiments.

2 Red blood cells

A healthy human RBC has a biconcave shape with an average diameter of approximately 8 μm. Figure 2 shows a schematic of a RBC membrane which consists of a lipid bilayer with an attached cytoskeleton formed by a network of the spectrin proteins linked by short filaments of actin. The lipid bilayer is considered to be a nearly viscous and area preserving membrane [6],

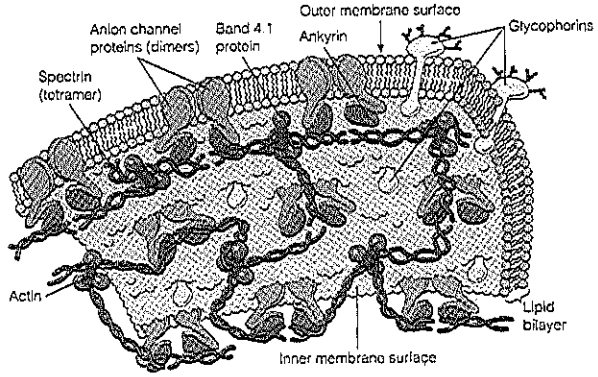

Fig. 2: *A schematic of the RBC membrane structure.*

while RBC elasticity is attributed to the attached spectrin network, as is the integrity of the entire RBC when subjected to severe deformations in the capillaries as small as 3 μm. The

RBC membrane encloses a viscous cytosol whose viscosity is several times larger than that of blood plasma under physiological conditions. Mechanical and rheological characteristics of RBCs and their dynamics are governed by: membrane elastic and viscous properties, bending resistance, and the viscosities of the external/internal fluids.

2.1 RBC membrane model

The RBC membrane shown in figure 3 is constructed by N_v particles $\{\mathbf{x}_{i=1...N_v}\}$ which correspond to a two-dimensional triangulated network [4, 7] on the RBC surface measured experimentally [8] and is given by

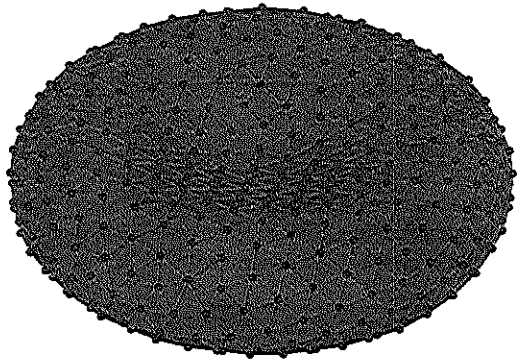

Fig. 3: *A sketch of a RBC membrane network.*

$$z = \pm D_0 \sqrt{1 - \frac{4(x^2+y^2)}{D_0^2}} \left[a_0 + a_1 \frac{x^2+y^2}{D_0^2} + a_2 \frac{(x^2+y^2)^2}{D_0^4} \right], \tag{1}$$

where $D_0 = 7.82\ \mu m$ is the average diameter, $a_0 = 0.0518$, $a_1 = 2.0026$, and $a_2 = -4.491$. The surface area and volume of this RBC are equal to 135 μm^2 and 94 μm^3, respectively.
The vertices of the network are connected by N_s springs with the following potential energy

$$V_s = \sum_{j \in 1...N_s} \left[\frac{k_B T l_m (3x_j^2 - 2x_j^3)}{4p(1-x_j)} + \frac{k_p}{(n-1) l_j^{n-1}} \right], \tag{2}$$

where l_j is the length of the spring j, l_m is the maximum spring extension, $x_j = l_j/l_m$, p is the persistence length, k_BT is the energy unit, k_p is the spring constant, and n is a power. The above equation consists of the attractive wormlike chain potential and a repulsive potential for $n > 0$ such that a non-zero equilibrium spring length can be imposed.
Membrane viscosity is incorporated into the RBC model through a dissipative force for each

and random $\mathbf{F}_{ij}^R$ forces, which satisfy the fluctuation-dissipation balance providing consistent temperature of the RBC membrane in equilibrium. The forces are as follows

$$\mathbf{F}_{ij}^D = -\gamma^T \mathbf{v}_{ij} - \gamma^C (\mathbf{v}_{ij} \cdot \mathbf{e}_{ij}) \mathbf{e}_{ij}, \tag{3}$$

$$\mathbf{F}_{ij}^R dt = \sqrt{2k_BT} \left(\sqrt{2\gamma^T} d\overline{\mathbf{W}}_{ij}^S + \sqrt{3\gamma^C - \gamma^T} \frac{tr[d\mathbf{W}_{ij}]}{3} \mathbf{1} \right) \cdot \mathbf{e}_{ij}, \tag{4}$$

where γ^T and γ^C are dissipative parameters, $\mathbf{v}_{ij}$ is the relative velocity of spring ends, $tr[d\mathbf{W}_{ij}]$ is the trace of a random matrix of independent Wiener increments $d\mathbf{W}_{ij}$, and $d\overline{\mathbf{W}}_{ij}^S = d\mathbf{W}_{ij}^S - tr[d\mathbf{W}_{ij}^S]\mathbf{1}/3$ is the traceless symmetric part.
The bending resistance of the RBC membrane is modeled by

$$V_b = \sum_{j \in 1...N_s} k_b \left[1 - cos(\theta_j - \theta_0) \right], \tag{5}$$

where k_b is the bending constant, θ_j is the instantaneous angle between two adjacent triangles having the common edge j, and θ_0 is the spontaneous angle.
Moreover, the RBC model requires the area and volume conservation constraints, which mimic area-incompressibility of the lipid bilayer and incompressibility of a cytosol, respectively. Such constraints are imposed as follows

$$V_{a+v} = \sum_{j \in 1...N_t} \frac{k_d (A_j - A_0)^2}{2A_0} + \frac{k_a (A - A_0^{tot})^2}{2A_0^{tot}} + \frac{k_v (V - V_0^{tot})^2}{2V_0^{tot}}, \tag{6}$$

where N_t is the number of triangles in the membrane network, A_0 is the triangle area, and k_d, k_a and k_v are the local area, global area and volume constraint coefficients, respectively. The terms A and V are the total RBC area and volume, while A_0^{tot} and V_0^{tot} are the specified total area and volume, respectively. More details on the RBC model can be found in [3, 4].

2.2 Membrane macroscopic properties and boundary conditions

Linear analysis of a regular hexagonal network allows us to uniquely relate the model parameters and the network macroscopic elastic properties (shear, area-compression, and Young's moduli), see [3, 4] for details. Thus, the membrane shear modulus is given by

$$\mu_0 = \frac{\sqrt{3} k_B T}{4 p l_m x_0} \left(\frac{x_0}{2(1-x_0)^3} - \frac{1}{4(1-x_0)^2} + \frac{1}{4} \right) + \frac{\sqrt{3} k_p (n+1)}{4 l_0^{n+1}}, \tag{7}$$

where l_0 is the equilibrium spring length and $x_0 = l_0/l_m$. The area-compression K and Young's Y moduli are equal to $2\mu_0 + k_a + k_d$ and $4K\mu_0/(K+\mu_0)$, respectively.
The relation between the model bending coefficient k_b and the macroscopic bending rigidity k_c of the Helfrich model [10] can be derived as $k_b = 2k_c/\sqrt{3}$ for a spherical membrane [4, 11]. This expression describes bending contribution of the energy in equation (5), but may not fully represent actual bending resistance of the RBC membrane since membrane bending may also result in local in-plane deformations.
The membrane shear viscosity η_m is related to the dissipative parameters γ^T, γ^C as $\eta_m = \sqrt{3}(\gamma^T + \gamma^C/4)$. Here γ^T accounts for a large portion of viscous contribution, and hence γ^C is set to $\gamma^T/2$ in all simulations.

In practice, the given macroscopic RBC properties serve as an input to be used to calculate the necessary mesoscopic model parameters from the equations above without any manual adjustment. A simulation of a RBC in equilibrium shows that the membrane may develop local bumps due to stress anomalies in a membrane triangulation since a network on a closed surface cannot consist of triangles whose edges have the same lengths. Such local stress artifacts depend on the network regularity and the ratio of the membrane elastic and bending contributions given by the Föppl-von Kármán number $\kappa = YR_0^2/k_c$, where $R_0 = \sqrt{A_0^{tot}/(4\pi)}$. To eliminate the stress artifacts we employ a *"stress-free"* model obtained by computational annealing. Thus, the equilibrium length l_0^i of each spring is set to the edge length after triangulation for $i = 1, \ldots, N_s$. This results in an individual maximum spring extension $l_m^i = l_0^i \times x_0$ (x_0 is a constant) and the spring parameters calculated for each spring using equation (7) for given μ_0. This modification provides a network free of local stress anomalies.
Both internal and external fluids are simulated by a collection of free particles and are separated by the RBC membrane through bounce-back reflections of them at a membrane surface. Moreover, a dissipative force between fluid particles and membrane vertices is set properly to account for the no-slip boundary conditions at the membrane surface. More details on boundary conditions can be found in [4, 11].

2.3 Membrane stretching

The modeled RBC is subjected to stretching analogous to that imposed on cells in optical tweezers experiments [12]. A stretching force F_s up to 200 pN is applied to the outermost $N_+ = \epsilon N_v$ vertices with the largest x coordinates in the positive x direction, and to the outermost $N_- = N_+$ vertices with the smallest x coordinates in the negative x direction, as shown in figure 4 (left). The vertex fraction ϵ is set to 0.02, corresponding to the contact diameter of an attached silica bead $d_c = 2\ \mu m$ used in the experiments.

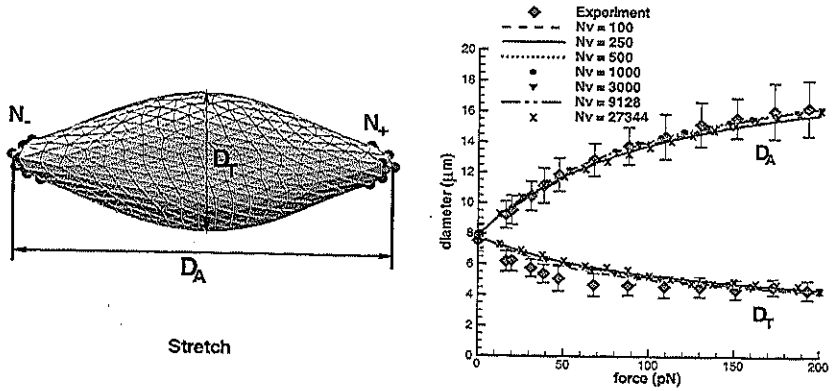

Fig. 4: *Schematic illustration of RBC deformation (left) and stretching response (right) for different number of vertices N_v in the network representation. The diamonds represent experimental results of Suresh et al. [12].*

For each external force, the cell is allowed to relax to an equilibrium stretched state. The axial diameter, D_A, defined as the maximum distance between the sets of points N_+ and N_-,

and the transverse diameter, D_T, defined as the maximum distance between two points from the set of all vertices projected on a plane perpendicular to the axial diameter, are averaged during a specified simulation time. Results presented in figure 4 (right) obtained with $\mu_0 = 6.3 \times 10^{-6}$ N/m are in good agreement with experimental data for all levels of coarse graining. Noticeable discrepancies for the transverse diameter may be due to experimental error. The optical measurements were performed from a single observation angle. Numerical simulations show that stretched cells may rotate in the yz plane. Consequently, measurements from a single observation angle are likely to underpredict the maximum transverse diameter.

2.4 Membrane rheology: twisting torque cytometry

In recent experiments, Puig-de-Morales-Marinkovic et al. [13] applied optical magnetic twisting cytometry (OMTC) to infer a dynamic complex modulus of the cell membrane. In this procedure, the cell membrane response is measured locally by observing the motion of an attached ferro-magnetic microbead driven by an oscillating magnetic field. The experiments have confirmed that the membrane is a viscoelastic material. Our viscoelastic membrane model will be tested against the results of optical magnetic twisting cytometry. The numerical simulations emulate the aforementioned experiments where the motion of a microbead attached to the top of the biconcave cell due an oscillating torque is studied, as shown in figure 5 (left). The data allow us to infer membrane properties such as the complex modulus.

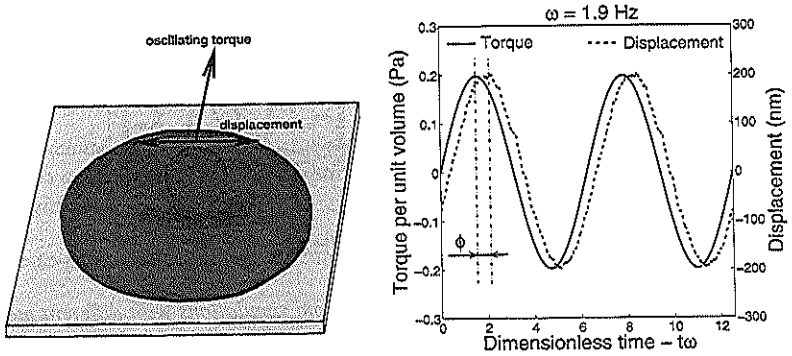

Fig. 5: *Illustration of the numerical setup of the twisting torque cytometry (left). Response of an attached microbead subject to an oscillating torque exerted on the bead (right).*

In the numerical model, the microbead is represented by a set of vertices deployed on a rigid sphere. A group of cell vertices near the bottom of the microbead simulates the area of attachment. The torque on the microbead is applied only to the bead vertices. Figure 5 (right) presents a typical response to an oscillating torque. The bead motion, monitored by the displacement of the center of mass, oscillates with the applied torque frequency. The oscillation is shifted by a phase angle, ϕ, that depends on the applied frequency. In the case of a purely elastic material and in the absence of inertia, the phase angle ϕ would be zero for any torque frequency.
The linear complex modulus of a viscoelastic material can be extracted from the phase angle

and torque frequency using the relations

$$g'(\omega) = \frac{\Delta T}{\Delta d}\cos\phi, \qquad g''(\omega) = \frac{\Delta T}{\Delta d}\sin\phi, \tag{8}$$

where $g'(\omega)$ and $g''(\omega)$ are two-dimensional storage and loss moduli and ΔT and Δd are the torque and bead displacement amplitudes. In the absence of inertia, the phase angle ϕ ranges between 0 and $\pi/2$.
Figure 6 compares the computed complex modulus with experimental data [13]. Good agreement is found for bending rigidity $k_c = 4.8 \times 10^{-19}$ J and membrane viscosity $\eta_m = 0.022$ Pa s. Since the Young's modulus of healthy RBCs is fixed by the cell stretching test, figure 6 essentially illustrates the dependence of g' on the membrane bending rigidity. To ensure good agreement with experiments, the bending rigidity of a healthy cell must be in the range 4 to 5×10^{-19} J, which is twice the widely adopted value, $k_c = 2.4 \times 10^{-19}$ J.

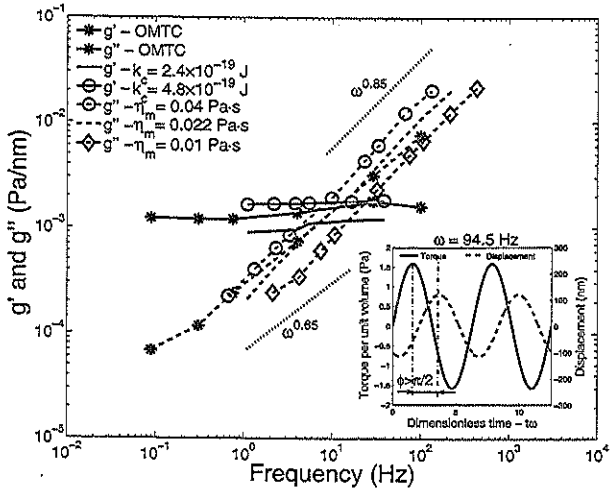

Fig. 6: *Graphs of the functions g' and g'' obtained from simulations with different membrane viscosities and bending rigidities. The numerical results are compared with experimental data by Puig-de-Morales-Marinkovic et al. [13]. The inset illustrates the effect of inertia for high frequencies of the driving torque.*

For small displacements, the loss modulus g'' depends mainly on the membrane viscosity and is insensitive to the membrane's elastic properties. The simulated loss modulus follows a power law in frequency with exponent $\alpha = 0.85$. In the experiments, the exponent is approximately 0.75. The agreement is fair in view of fitting errors in only two frequency decades in simulations and experiments. The inset in figure 6 shows that inertial effects affect g' at high frequencies. Decreasing the bead mass would allow us to obtain rheological data for higher torque frequencies, but the computational cost is high since a small time step is required. When the loss modulus dominates the storage modulus, the bead-displacement amplitude at fixed torque amplitude is extremely small and hard to measure in the laboratory. However, bead displacements in simulations can be successfully detected on a scale of several nanometers.

2.5 Tube flow

The mean velocity of Poiseuille flow in a circular tube is defined as

$$\bar{v} = \frac{1}{S}\iint v(r)\,\mathrm{S}, \tag{9}$$

where S is the cross-sectional area and $v(r)$ is the axial velocity. For a Newtonian fluid, $\bar{v} = v_c/2$, where v_c is the centerline velocity.
At low flow rates, a RBC suspended in tube flow retains its biconcave shape. As the driving pressure gradient increases, the cell obtains the parachute-like shape shown in figure 7 (left) for a tube with diameter $9\mu m$, in agreement with experimental observations [14]. To identify the

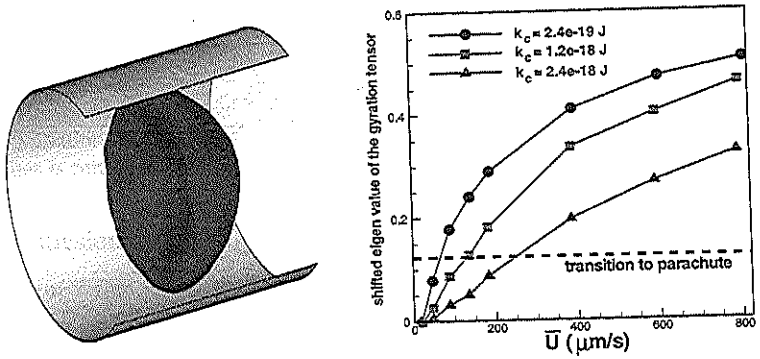

Fig. 7: *Parachute shape of a cell suspended in Poiseuille flow through a $9\mu m$ diameter tube (left). Excess axial eigenvalue of the gyration tensor above that for a biconcave disk for different bending rigidities (right).*

biconcave-to-parachute transition, we compute the gyration tensor

$$G_{mn} = \frac{1}{N_v}\sum_i (r_m^i - r_m^C)(r_n^i - r_n^C), \tag{10}$$

where r^i are the membrane vertex coordinates, r^C is the membrane center of mass, and m, n stand for x, y, or z. The eigenvalues of the gyration tensor allow us to characterize the cell shape. For the equilibrium biconcave shape, the gyration tensor has two large eigenvalues corresponding to the midplane of the biconcave disk, and one small eigenvalue corresponding to the disk thickness. At the biconcave-to-parachute transition, the small eigenvalue increases indicating that the cell elongates along the tube axes.
Figure 7 (right) illustrates the dependence of the axial eigenvalue on the mean flow velocity for different membrane bending rigidities. The dashed line describes the biconcave-to-parachute transition. For healthy cells, the transition occurs at a mean velocity of about 65 μm/s. The transition for larger bending rigidity occurs at stronger flows. The critical mean velocity changes almost linearly with the bending rigidity k_c. These results are consistent with numerical simulations by Noguchi & Gompper [15].

Next we model blood flow in tubes . Blood is simulated with a number of RBCs suspended in a solvent. The flow property of interest is the relative apparent viscosity of the RBC suspension defined as

$$\lambda_{app} = \frac{\eta_{app}}{\eta_o}, \qquad \eta_{app} = \frac{nfR_0^2}{8\bar{u}}, \tag{11}$$

where n is the suspension number density, f is the force exerted on each particle, R_0 is the tube radius, η_o is the solvent viscosity, and $\bar{u}$ is the bulk velocity calculated using equation (9). The product nf is the streamwise pressure gradient, $\Delta P/L$, where L is the tube length.
The inset plot of figure 8 shows a sample snapshot of blood flowing in a tube of diameter $D = 20\ \mu m$ after steady state is achieved. We observe a RBC core formation with a thin plasma layer next to the tube walls. Figure 8 presents the relative apparent blood viscosity for

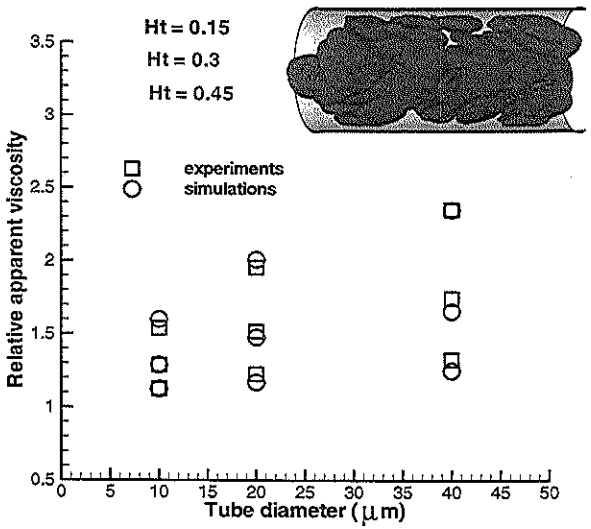

Fig. 8: *Relative apparent viscosity in comparison with experimental data [16] for different hematocrit values and tube diameters. The inset plot shows a snapshot of RBCs in Poiseuille flow in a tube of a diameter* $D = 20\ \mu m$ *at hematocrit* 0.45.

different hematocrit values (H_t) and tube diameters in comparison with experiments [16]. The apparent blood viscosity decreases with tube diameter which is called the Fahraeus-Lindqvist effect [17] found in experiments of blood flow in glass tubes. RBCs in tube flow migrate to the tube center yielding a cell-free layer (CFL) near the wall absent of RBCs. The fluid viscosity of the CFL region is much smaller than that of the tube core populated with RBCs providing an effective lubrication for the core to flow. The thickness of the CFL is directly related to the Fahraeus-Lindqvist effect. Thus, in small tubes the CFL thickness is significant with respect to the tube diameter resulting in a smaller relative apparent viscosity in comparison with that in larger tubes, where the CFL thickness becomes negligible with respect to the tube diameter.

3 White blood cells

Leukocytes or WBCs have a more complex structural organization than RBCs, see figure 1. In comparison with RBCs, WBCs contain the nucleus characterized by low deformability, a complex cytoplasm with many organelles, and the cytoskeleton, which connects the cell membrane, cytoplasm, and nucleus. WBCs are less deformable than RBCs and are spherical in shape with diameter between 7 μm and 20 μm. However, WBCs are also able to undergo significant deformation when entering the smallest blood capillaries.
WBCs may adhere to the vascular endothelium , which is important for their physiological function in the immune response. WBC adhesion is mediated by receptors concentrated on a small area of microvilli tips [20], which are observed as the ruffles [18, 19] on the WBC surface. These receptors are known to be from the selectin family and have fast association and dissociation kinetics [21], which facilitates WBC adhesion even under fast blood flow conditions. Trajectories of a rolling adhered WBCs are often characterized by a "stop-and-go" motion rather than rolling with a constant velocity along the vessel wall [22, 23]. The sporadic rolling behavior is attributed to a stochastic nature of formation and dissociation of receptor-ligand bonds. However, at high shear rates WBC rolling was observed to be less erratic and shows smaller variations in rolling velocity than at low shear rates [23]. In addition, rolling at high shear rates is further stabilized by an increase in the number of receptor-ligand bonds [23].

3.1 Adhesion model

Adhesion of WBCs to endothelium is mediated by the interactions between receptors and ligands which are the adhesion sites distributed on a cell and a wall, respectively. Figure 9 shows a sketch of a WBC with surface receptors and ligands distributed uniformly on the wall. A po-

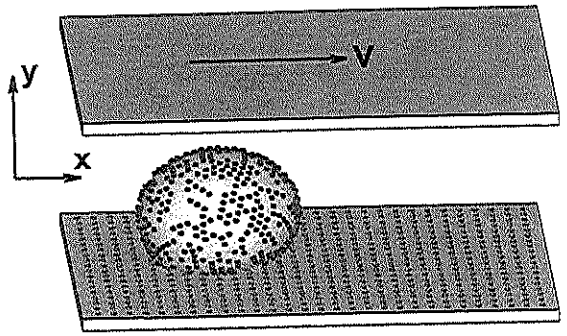

Fig. 9: *A sketch of a modeled WBC above the lower wall. Receptors are drawn in blue and ligands in red.*

tential bond between a receptor and a ligand may be formed only if the receptor is close enough to the free ligand, which is characterized by the reactive distance d_{on}. A ligand is called free if it is not bound to any receptors. During the time a receptor is within the distance d_{on} to a free ligand, a bond can be formed with on-rate k_{on}. Reversely, existing bonds are ruptured with

off-rate k_{off} or if their length exceeds the rupture distance d_{off}. The rates k_{on} and k_{off} are defined as follows

$$k_{on} = k_{on}^0 \exp\left(-\frac{\sigma_{on}(l-l_0)^2}{2k_BT}\right), \qquad k_{off} = k_{off}^0 \exp\left(\frac{\sigma_{off}(l-l_0)^2}{2k_BT}\right), \tag{12}$$

where k_{on}^0 and k_{off}^0 are the reaction rates at the distance $l = l_0$ between a receptor and a ligand with the equilibrium spring length l_0 defined below. The effective on and off strengths σ_{on} and σ_{off} define a decrease or an increase of the corresponding rates within the interaction lengths d_{on} and d_{off}, and k_BT is the unit of energy. The force exerted on the receptors and ligands by an existing bond is given by

$$F(l) = k_s(l - l_0), \tag{13}$$

where k_s is the spring constant. The probabilities of bond formation and dissociation are defined as $P_{on} = 1 - \exp(-k_{on}\Delta t)$ and $P_{off} = 1 - \exp(-k_{off}\Delta t)$, where Δt is the time step in simulations. This adhesion model is a slight modification of the well-known adhesive dynamics model developed by Hammer and Apte [24]. In their model $\sigma_{on} = \sigma_{ts}$ and $\sigma_{off} = k_s - \sigma_{ts}$, where σ_{ts} is the transition state spring constant.

During the course of a simulation the receptor/ligand interactions are considered every time step. First, all existing bonds between receptors and ligands are checked for a potential dissociation according to the probability P_{off}. A bond is ruptured if $\xi < P_{off}$ and left unchanged otherwise, where ξ is a random variable uniformly distributed on $[0, 1]$. If a bond is ruptured the corresponding ligand is available for new binding. Second, all free ligands are examined for possible bond formations. For each free ligand we loop over the receptors within the distance d_{on}, and bond formation is attempted for each found receptor according to the probability P_{on}. This loop is terminated when a bond is formed. Finally, the forces of all remaining bonds are calculated and applied.

Note that this algorithm permits only a single bond per ligand, while receptors may establish several bonds if several ligands are free within their reaction radius. This provides an additional capability for the adhesive dynamics model compared with that employing one-to-one interactions between receptors and ligands. Also, this assumption appears to furnish a more realistic representation of adhesive interactions of WBCs with a wall, since leukocyte membrane has a number of microvilli, where the receptors that mediate cell adhesion are clustered.

3.2 WBC adhesive dynamics

Modeling of WBC adhesive dynamics shows different types of cell behavior such as firm adhesion, continuous rolling over a wall, and rolling in a "stop-and-go" manner. Cytoadhesive dynamics depends on a number of factors such as density and distribution of the available receptors and ligands, their interactions (e.g., bond formation/dissociation rates, bond strength), cell properties (e.g., cell shape, elasticity, bending rigidity), and flow conditions (e.g., shear rate, shear stress). The effect of some of those conditions will be examined next.

The simulations of WBC adhesive dynamics are performed for ranges of unstressed on and off rates. Similar ranges were considered in [25] for the adhesive dynamics of a solid spherical particle. Several states of WBC adhesive dynamics can be defined based on the average cell velocity $\bar{v}_c$ and pause time $\bar{\tau}_p$. The average pause time is calculated from the time sequence $\{\Lambda_i\}_{i=1...T}$ of WBC motion defined as

$$\Lambda_i = \begin{cases} 1 & \text{if } v_c^i > 0.01V_m, \quad \text{in motion} \\ 0 & \text{if } v_c^i \le 0.01V_m, \quad \text{arrest} \end{cases}, \tag{14}$$

where i denotes a step in time, T is the total number of steps, V_m is the flow velocity at the channel center, and $v_c^i = (x_c^i - x_c^{i-1})/\Delta t$ is the WBC center-of-mass velocity while x_c^i is the cell center-of-mass and Δt is the time interval. This sequence is then analyzed to calculate the average length of an arrest (average pause time) which is equivalent to the average length of continuous subsequences of zeros multiplied by Δt. The average cell velocity is defined as follows

$$\bar{v}_c = \frac{1}{T-1}\sum_{i=2}^{T} v_c^i. \tag{15}$$

The WBC dynamics is divided into four states according to the average pause time $\bar{\tau}_p$ and cell velocity $\bar{v}_c$:

1) *Firm adhesion:* the state of the WBC arrest which is characterized by $\bar{\tau}_p > 0.5\ s$. Infrequent small jumps in the cell velocity are possible due to rare bond dissociation.

2) *Stop-and-go rolling:* the cell motion is described by frequent interchanges between WBC arrest and mobility. This state is defined by $0.1\ s < \bar{\tau}_p \le 0.5\ s$.

3) *Stable rolling:* the state corresponds to WBC motion with a relatively stable rolling velocity. It is established if $\bar{\tau}_p \le 0.1\ s$ and $\bar{v}_c < 0.8V_m$.

3) *Free motion:* the WBC is moving freely with the channel flow, when adhesion interactions are not able to resist a lift on the cell due to hydrodynamic flow. This state is characterized by $\bar{\tau}_p \le 0.1\ s$ and $\bar{v}_c \ge 0.8V_m$.

The time interval is chosen to be $\Delta t = 0.01\ s$. The simulations are run for $10\ s$, while data analysis is performed for times after $1\ s$ to exclude flow startup effects.

Figure 10 presents the center-of-mass displacements (x_c) and velocities (v_c) for different WBC adhesion states. The "A" plots show that firm adhesion is characterized by relatively long times of cell arrests. However, rare events of sudden motion may be present due to erratic bond dissociation. They are represented by several submicron steps in the WBC displacement and the corresponding peaks in the cell velocity shown in figure 10 "A". Note that WBC velocity fluctuates around the zero value and frequently displays small negative values; however, no net motion in the negative x direction is observed. This may be due to the presence of thermal fluctuations and/or a retraction of a WBC and its bonds to the wall after deformation by the flow, since the center-of-mass velocity is measured based on current and previous positions with the time interval $\Delta t = 0.01\ s$. The stop-and-go rolling shown in figure 10 "B" is well described by a staircase-like displacement directly related to frequent peaks in the cell velocity and intermittent WBC stops. In contrast, stable rolling is characterized by a near linear WBC displacement shown in figure 10 "C". Finally, under free motion (fig. 10 "D") WBCs move in shear flow near the channel center with the average velocity slightly lower than $V_m = 1500\ \mu m/s$. The adhesive interactions are not strong enough to counterbalance cell-wall hydrodynamic interactions, which force WBCs to migrate to the channel center. After WBC detachment from the wall, no further interaction with the wall is encountered.

Figure 11 shows the WBC adhesion dynamics states for wide ranges of unstressed on (k_{on}^0) and off (k_{off}^0) rates normalized by the flow shear rate. This plot is called *on-off state diagram* similar to that by Korn and Schwarz [25]. Firm adhesion occurs if the bond dissociation rate is small. Under this condition bond rupture is a rare event, while bonds are formed with a faster rate to keep a WBC in arrest. At low values of k_{on}^0 the border between firm adhesion and stop-and-go

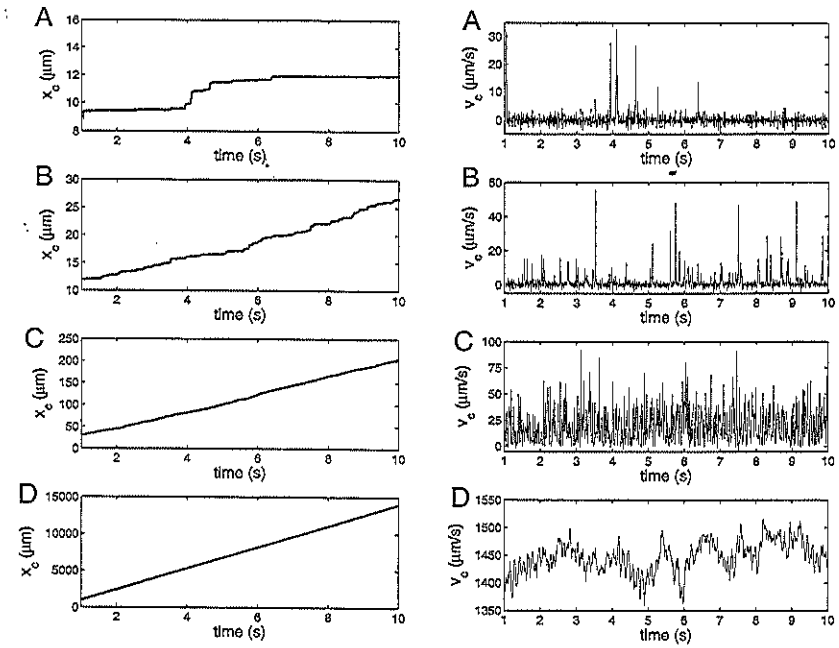

Fig. 10: *Center-of-mass displacements (x_c) and velocities (v_c) for various adhesion states of a WBC. A - firm adhesion, B - stop-and-go rolling, C - stable rolling, and D - free motion.*

rolling motion (black dashed line in figure 11) is achieved by a proper balance between the association and dissociation rates. However, this border shows no dependence on the rate k_{on}^0 at its high values. This behavior is due to a limited number of available receptors and ligands for binding. Thus, if there are no free receptors or analogously no free ligands left for binding, a further increase of k_{on}^0 will have no effect on the firm adhesion of a WBC.

As we increase the bond dissociation rate k_{off}^0 for a fixed k_{on}^0, WBC firm adhesion transits into the stop-and-go rolling state. Note that this behavior is observed in a thin stripe region of the on-off state diagram in figure 11 right above the "firm adhesion" region. In light of this, the stop-and-go rolling can also be thought of as an unstable firm adhesion. Hence, if the rate k_{off}^0 becomes significant enough in comparison with k_{on}^0 to allow relatively frequent random ruptures of bonds, a WBC is subject to a stop-and-go motion characterized by step-like displacements and velocity jumps shown in figure 10 "B".

Upon a further increase in k_{off}^0 with respect to k_{on}^0 a WBC shows stable rolling or detaches from the wall and undergoes a free motion in the flow. Note that stable rolling is only possible if the association rate is large enough to facilitate fast bond formation. Thus, stable WBC rolling on the wall can be described by a dynamic rupture of bonds at the back of the cell contact area and their quick formation at the front of a WBC. Figure 11 shows that for small k_{on}^0 values, a WBC

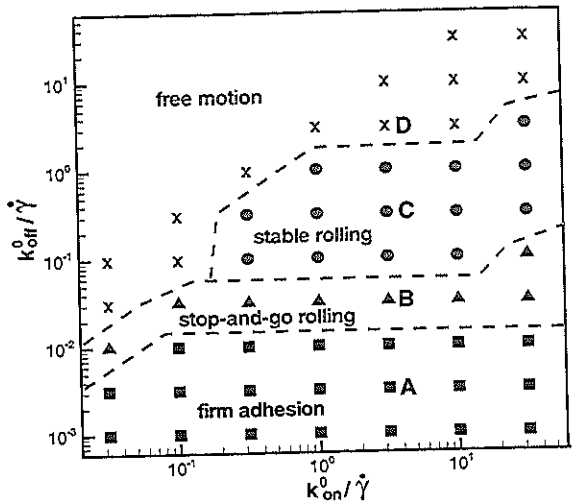

Fig. 11: *On-off state diagram of WBC adhesion dynamics states: firm adhesion (squares), stop-and-go rolling (triangles), stable rolling (circles), and free motion (crosses). The letters "A-D" mark simulations shown in figure 10. Dashed lines are drawn for the eye to identify regions corresponding to different states.*

transits into a free motion above the border of the stop-and-go rolling region (blue dashed line). In addition, a WBC detaches from the wall if the bond dissociation rate becomes comparable with the rate of bond formation.

4 Summary

Numerical simulations of blood cells and blood flow have shown a tremendous advancement in recent years allowing for a realistic and quantitative description of blood flow and blood related processes. The presented RBC model is able to accurately capture RBC mechanics, rheology, and dynamics. The membrane skeleton is constructed as a network of interconnected viscoelastic springs that provide RBC elasticity analogously to the spectrin network, and viscous dissipation similarly to that in the lipid bilayer. This network also incorporates the membrane bending rigidity to mimic bending resistance of the lipid bilayer. In addition, local and global area constraints ensure the membrane incompressibility of real RBCs, while the volume constraint ensures the incompressibility of the inner solvent.

Adhesive dynamics of WBCs can be captured using the stochastic bond formation/dissociation model, which is able to reproduce several states of WBC adhesion in flow such as firm adhesion, stop-and-go rolling, and stable rolling. The predictions are in quantitative agreement with recent experimental observations and the modeling method for blood cells and blood flow provides new capabilities for guiding and interpreting future *in vitro* and *in vivo* studies and may aid to

obtain realistic predictions of blood flow in microcirculation and in microfluidic devices.

Appendices

A Dissipative particle dynamics

Dissipative particle dynamics (DPD) [5,26] is a mesoscopic particle method, where each particle represents a *molecular cluster* rather than an individual atom, and can be thought of as a soft lump of fluid. The DPD system consists of N point particles of mass m_i, position $\mathbf{r}_i$ and velocity $\mathbf{v}_i$. DPD particles interact through three forces: conservative ($\mathbf{F}^C_{ij}$), dissipative ($\mathbf{F}^D_{ij}$), and random ($\mathbf{F}^R_{ij}$) forces given by

$$\mathbf{F}^C_{ij} = F^C_{ij}(r_{ij})\hat{\mathbf{r}}_{ij}, \qquad \mathbf{F}^D_{ij} = -\gamma\omega^D(r_{ij})(\mathbf{v}_{ij}\cdot\hat{\mathbf{r}}_{ij})\hat{\mathbf{r}}_{ij}, \qquad \mathbf{F}^R_{ij} = \sigma\omega^R(r_{ij})\frac{\xi_{ij}}{\sqrt{dt}}\hat{\mathbf{r}}_{ij}, \tag{16}$$

where $\hat{\mathbf{r}}_{ij} = \mathbf{r}_{ij}/r_{ij}$, and $\mathbf{v}_{ij} = \mathbf{v}_i - \mathbf{v}_j$. The coefficients γ and σ define the strength of dissipative and random forces, respectively. In addition, ω^D and ω^R are weight functions, and ξ_{ij} is a normally distributed random variable with zero mean, unit variance, and $\xi_{ij} = \xi_{ji}$. All forces are truncated beyond the cutoff radius r_c. The conservative force is given by

$$F^C_{ij}(r_{ij}) = a_{ij}(1 - r_{ij}/r_c) \quad \text{for} \quad r_{ij} \le r_c, \tag{17}$$

where a_{ij} is the conservative force coefficient between particles i and j. The random and dissipative forces form a thermostat and must satisfy the fluctuation-dissipation theorem in order for the DPD system to maintain equilibrium temperature T [27]. This leads to

$$\omega^D(r_{ij}) = \left[\omega^R(r_{ij})\right]^2, \qquad \sigma^2 = 2\gamma k_B T, \tag{18}$$

where k_B is the Boltzmann constant. The choice for the weight functions is as follows

$$\omega^R(r_{ij}) = (1 - r_{ij}/r_c)^k \quad \text{for} \quad r_{ij} \le r_c, \tag{19}$$

where k is an exponent. The time evolution of velocities and positions of particles is determined by the Newton's second law of motion

$$d\mathbf{r}_i = \mathbf{v}_i dt, \qquad d\mathbf{v}_i = \frac{1}{m_i}\sum_{j\neq i}\left(\mathbf{F}^C_{ij} + \mathbf{F}^D_{ij} + \mathbf{F}^R_{ij}\right)dt. \tag{20}$$

The above equations of motion are integrated using the modified velocity-Verlet algorithm [26].

References

[1] T. A. Springer, *Ann. Rev. Physiol.* **57**, 827 (1995).

[2] E. B. Finger, K. D. Puri, R. Alon, M. B. Lawrence, U. H. von Andrian, and T. A. Springer, *Nature (London)* **379**, 266 (1996).

[3] D. A. Fedosov, B. Caswell, and G. E. Karniadakis, *Comp. Meth. App. Mech. Eng.* **199**, 1937 (2010).

[4] D. A. Fedosov, B. Caswell, and G. E. Karniadakis, *Biophys. J.* **98**, 2215 (2010).

[5] P. J. Hoogerbrugge and J. M. V. A. Koelman, *Europhys. Lett.* **19**, 155 (1992).

[6] Y. C. Fung, *Biomechanics: Mechanical properties of living tissues* (Springer-Verlag, New York, 1993)

[7] D. E. Discher, D. H. Boal, and S. K. Boey, *Biophys. J.* **75**, 1584 (1998).

[8] E. A. Evans and R. Skalak, *Mechanics and thermodynamics of biomembranes* (CRC Press, Inc., Boca Raton, Florida, 1980)

[9] P. Espanol, *Phys. Rev. E* **57**, 2930 (1998).

[10] W. Helfrich, *Z. Naturforschung C* **28**, 693 (1973).

[11] D. A. Fedosov, *Multiscale modeling of blood flow and soft matter* (PhD thesis, Brown University, Providence, USA, 2010)

[12] S. Suresh, J. Spatz, J. P. Mills, A. Micoulet, M. Dao, C. T. Lim, M. Beil, and T. Seufferlein, *Acta Biomaterialia* **1**, 15 (2005).

[13] M. Puig-de-Morales-Marinkovic, K. T. Turner, J. P. Butler, J. J. Fredberg, and S. Suresh, *Am. J. Physiol.: Cell Physiol.* **293**, 597 (2007).

[14] K. Tsukada, E. Sekizuka, C. Oshio, and H. Minamitani, *Microvasc. Res.* **61**, 231 (2001).

[15] H. Noguchi and G. Gompper, *Proc. Natl. Acad. Sci. USA* **102**, 14159 (2005).

[16] A. R. Pries, D. Neuhaus, and P. Gaehtgens, *Am. J. Physiol.* **263**, H1770 (1992).

[17] R. Fahraeus and T. Lindqvist, *Am. J. Phys.* **96**, 562 (1931).

[18] S. L. Erlandsen, S. R. Hasslen, and R. D. Nelson, *J. Histochem. Cytochem.* **41**, 327 (1993).

[19] K. L. Moore, K. D. Patel, R. E. Bruehl, F. Li, D. A. Johnson, H. S. Lichenstein, R. D. Cummings, D. F. Bainton, and R. P. McEver, *J. Cell Biol.* **128**, 661 (1995).

[20] U. H. von Andrian, S. R. Hasslen, R. D. Nelson, S. L. Erlandsen, and E. C. Butcher, *Cell* **82**, 989 (1995).

[21] M. B. Lawrence and T. A. Springer, *Cell* **65**, 859 (1991).

[22] R. Alon, D. A. Hammer, and T. A. Springer, *Nature (London)* **374**, 539 (1995).

[23] S. Chen and T. A. Springer, *J. Cell Biol.* **144**, 185 (1999).

[24] D. A. Hammer and S. M. Apte, *Biophys. J.* **63**, 35 (1992).

[25] C. B. Korn and U. S. Schwarz, *Phys. Rev. E* 77, 041904 (2008).

[26] R. D. Groot and P. B. Warren, *J. Chem. Phys.* **107**, 4423 (1997).

[27] P. Espanol and P. Warren, *Europhys. Lett.* **30**, 191 (1995).